Delft University of Technology

Delft Center for Systems and Control

Technical report 23-017

Model predictive control of a thermal chimney and dynamic solar shades for an all-glass facades building*

L.A. de Araujo Passos, T.J. Ceha, S. Baldi, and B. De Schutter

If you want to cite this report, please use the following reference instead:
L.A. de Araujo Passos, T.J. Ceha, S. Baldi, and B. De Schutter, "Model predictive control of a thermal chimney and dynamic solar shades for an all-glass facades building," *Energy*, vol. 264, p. 126177, Feb. 2023. doi:10.1016/j.energy.2022.126177

Delft Center for Systems and Control
Delft University of Technology
Mekelweg 2, 2628 CD Delft
The Netherlands
phone: +31-15-278.24.73 (secretary)
URL: https://www.dcsc.tudelft.nl

* This report can also be downloaded via https://pub.bartdeschutter.org/abs/23_017.html

Model predictive control of a thermal chimney and dynamic solar shades for an all-glass facades building

Luigi Antonio de Araujo Passos[a], Thomas Joseph Ceha[a], Simone Baldi[b,a,*] and Bart De Schutter[a]

[a] Delft Center for Systems and Control, Delft University of Technology, the Netherlands
[b] School of Mathematics, Southeast University, Nanjing, China

Abstract

Controlling the operation of HVAC (Heating, Ventilation, and Air-Conditioning) systems is arguably the most effective way to reach desired indoor conditions in buildings. Nevertheless, such control may involve complex dynamics when dealing with passive energy technologies. In this paper, we focus on maximizing the passive operation of HVAC in a novel low-energy building design by means of Model Predictive Control (MPC). The low-energy building design, located in The Green Village, consists of a thermal chimney and solar shades over all-glass facades to provide the required indoor air conditioning as passively as possible. The MPC controller is based on a transient grey box model and a hierarchical control architecture to satisfy thermal comfort while minimizing the active energy requirements. Using sensor data collected from the actual building in April and May 2021, the grey box model shows a good agreement with the measurements, since the variance accounted for is 90% in most cases. Moreover, via a comparative study among different MPC architectures we show that managing the distinct transient response of each component (shades and chimney) is the best for successful overall performance — e.g., considering linear agents for shading and nonlinear agents for ventilation. The hierarchical MPC architecture established outperforms the standard ones by 22.7% in terms of control performance. We also compare the proposed MPC approach against the rule-based control method currently implemented in the actual building, which indicates that MPC demands about 78% less active energy, highlighting the proposed optimization-based control approach.

Keywords: MPC (Model Predictive Control), HVAC (Heating, Ventilation, and Air-Conditioning), passive energy, solar shading, thermal chimney, all-glass facades.

*Corresponding author: S. Baldi (s.baldi@tudelft.nl)

Nomenclature

$\mathcal{A}$	Matrix of linear coefficients [-]
A	Heat transfer area [m^2]
$\mathcal{B}$	Matrix of linear coefficients [-]
c	Specific heat at constant pressure [J/(kgK)]
C	Heat capacity [J/K]
$\mathcal{C}$	Output matrix [-]
C_d	Friction coefficient [-]
d	Vector of disturbances [-]
$\mathcal{E}$	Matrix of linear coefficients [-]
F	View factor [-]
g	Gravitational constant [m/s^2]
h	Convection coefficient [$W/(m^2K)$]
H	Distance between tower inlet and outlet [m]
I	Solar irradiance [W/m^2]
$\mathcal{K}$	Kalman filter matrix [-]
L	Thickness of insulation
m	Mass [kg]
N	Time horizon [s]
$\mathcal{P}$	Penalization coefficients [-]
q	Heat [J]
$\mathcal{Q}$	Penalization coefficients [-]
$\mathcal{R}$	Penalization coefficients [-]
t	Time [s]
T	Temperature [K]
u	Control inputs [-]
v	Sensor disturbances [-]
w	White noise [-]
x	Linearized temperature states [K]
X	Length [m]
Y	Width [m]
y_p	System output [K]
Z	Depth [m]

Greek letters

α	Solar absorptance [-]
ε	Emissivity [-]
κ	Conduction coefficient [W/(mK)]
λ	Linear irradiation coefficient [$W/(m^2K^4)$]
ξ	Parameter for floor shading [-]
ρ	Specific mass [kg/m^3]
τ	Solar transmittance [-]
φ	Chimney cross-sectional area [m^2]

Subscripts

a	Indoor air
c_1, c_2	Ceiling layers
e	East
e	Electric backup
est	Estimated
f_1, f_2	Floor layers
g	Outside ground
hp	Heat pump
mod	Model
n	North
o	Outside air
p	People
ref	Reference
s	Solid surfaces
s	South
s	Shades
sky	Sky
v	Ventilation
w	West
w_1, w_2, w_3	Glass layers

Superscripts

k	Time step

1 Introduction

Passive energy technologies have been encouraged for different applications, including HVAC (Heating, Ventilation, and Air-Conditioning) in low-energy buildings [1]. The positive impact of such technologies is particularly relevant for office buildings, where the stricter working period and high occupancy require significant energy consumption to meet the indoor thermal comfort [2]. Additionally, the recent COVID-19 outbreak urges for higher ventilation in public buildings, and therefore, higher energy demand [3]. The use of passive energy technologies, however, calls for the integration of such technologies with an effective control scheme for reducing the requirements of active energy. Reaching this integration has stimulated investigations on optimal passive design parameters in different climates [4].

Among different options, shading systems have been widely suggested as passive energy technologies since the solar heat load plays a role in indoor air temperature profile and HVAC demand [5]. The shading of facades has shown to be a promising technology for heating, cooling, and day-lighting control [6]: in fact, the operation of shadings can be calibrated dynamically according to the targeted purpose, e.g., using solar-tracked surfaces to enhance heat gains [7] or to prioritize daylighting [8]. Although some software considers shadings in its library of components [9], the literature suggests further efforts to optimize the shadings operation [10]. Natural ventilation systems represent another popular class of passive energy technologies. They have been studied via a variety of components such as thermal chimneys and wind towers [11]. Thermal chimneys are the most notorious, while more studies combining other natural ventilation sources are still required for effective applicability in buildings [12], and further studies for the optimization and control of thermal chimneys are recommended in the literature [13].

Many control methods have been considered putting emphasis on the optimal operation of dynamic low-energy systems, which includes MPC (Model Predictive Control) as a state-of-the-art approach [14]. MPC relies on optimization algorithms and on the knowledge of the system behavior to predict and select the best control inputs at each time step [15]. In this sense, MPC has been suggested for the real-time optimization of radiant floors [16], natural ventilation [17], shading systems [18], thermal energy storage [19], energy use in smart buildings [20], and integration of multiple HVAC systems [21]. Furthermore, MPC has been studied in the integration of electricity and heat systems [22], and demand response in residential air-conditioning [23].

The MPC methodology is flexible and allows considering constraints, deterministic models [24], stochastic scenarios, nonlinear models [25], and can incorporate deep learning [26]. Demonstrations in functional buildings have also been reported, e.g., a cloud-based, white-box MPC for a ground-sourced heat pump in offices [27], fuzzy nonlinear MPC [28], and zone-based MPC to supply heating and electricity in an academic building [29].

The literature on MPC is vast since the method encompasses the optimization of a wide range of systems. Generally, HVAC systems exhibit improved thermo-economic performance when controlled by MPC as compared to rule-based or state-of-the-art control methods [30]. However, there is no ultimate consensus in the literature about the most effective way to implement MPC in each specific system, especially when considering the optimization of complex fully passive heating and ventilation systems: a set of questions arises concerning the benefits in system performance, the most proper control architecture configuration, the most proper cost function to maintain comfort while saving energy, the effects of the models' nonlinearities, etc. Finding answers to these questions may facilitate the practical application of MPC in novel low-energy building designs [31].

This article explores MPC to optimally integrate passive heating and ventilation while drawing on a unique all-glass facade building with steerable solar shadings and a thermal chimney. Such design relies on an actual building located in The Green Village as a research facility [32, 33]. The system configuration involves a case study about maximizing the use of passive energy technologies in meeting centers, relying on architectural designs such as natural ventilation, structural glasses, and dynamic solar shadings. To promote the viability of such passive technologies on a larger scale, we suggest an optimized model-based control approach to maximize the use of passive energy and, consequently, the feasibility of the technologies studied, since the system performance is enhanced. The optimized control aspect arises because, differently from standard MPC architectures (either linear or nonlinear), in this paper we develop a novel grey-box hierarchical MPC architecture that manages the passive heating and ventilation processes accordingly to their distinct heat capacities and passivity — for instance, considering linear agents for shadings and nonlinear agents for ventilation. Furthermore, we compare the proposed MPC controller to the rule-based PID controller operating in the real building. The novelties of this work can be outlined as follows:

- Providing an appropriate modeling approach for a real-life fully passive heating and ventilation system. The system is located in The Green Village and the models were validated with 35 temperature sensors.
- The optimization problem must be designed to fit the need of the fully passive system. For this purpose, we provide a study of the objective functions for maximizing passive energy use while meeting thermal comfort, studying the combination of optimized parameters, studying the Pareto curves, and studying the constraints.
- Clearly, the control must be applied in the real system: for this purpose, we perform an extensive comparison of 3 MPC architectures in terms of computation time and accuracy for optimal control of passive energy systems for the real-life application under consideration.
- Analogously, we provide a comparison of MPC and PID controllers in terms of energy savings and control profiles for optimal strategy.
- We show reduced energy consumption of a novel system configuration toward zero-energy buildings using hierarchical MPC.

The rest of the paper presents the system description and modeling in Section 2, followed by the control design and proposed MPC structures in Section 3. The experiment results and discussions are in Section 4, followed by the conclusions in Section 5.

2 Thermal system description and modeling

The thermal system under consideration deploys passive energy through the combination of two subcomponents: a thermal chimney for buoyancy-driven ventilation, and transparent all-glass facades for solar heating. Such configuration is based on the actual building installed in The Green Village [32, 33], at Delft University of Technology, in the Netherlands. As shown in Figure 1, in this system external steerable shades cover the vertical facades for controlling the solar irradiance hitting the building. The thermal chimney is assisted by backup fans and a heat pump to supply the airflow rates and temperatures desired. The drilled deck floor plays a crucial role in this configuration, since it drags the air flowing into the building, and may absorb

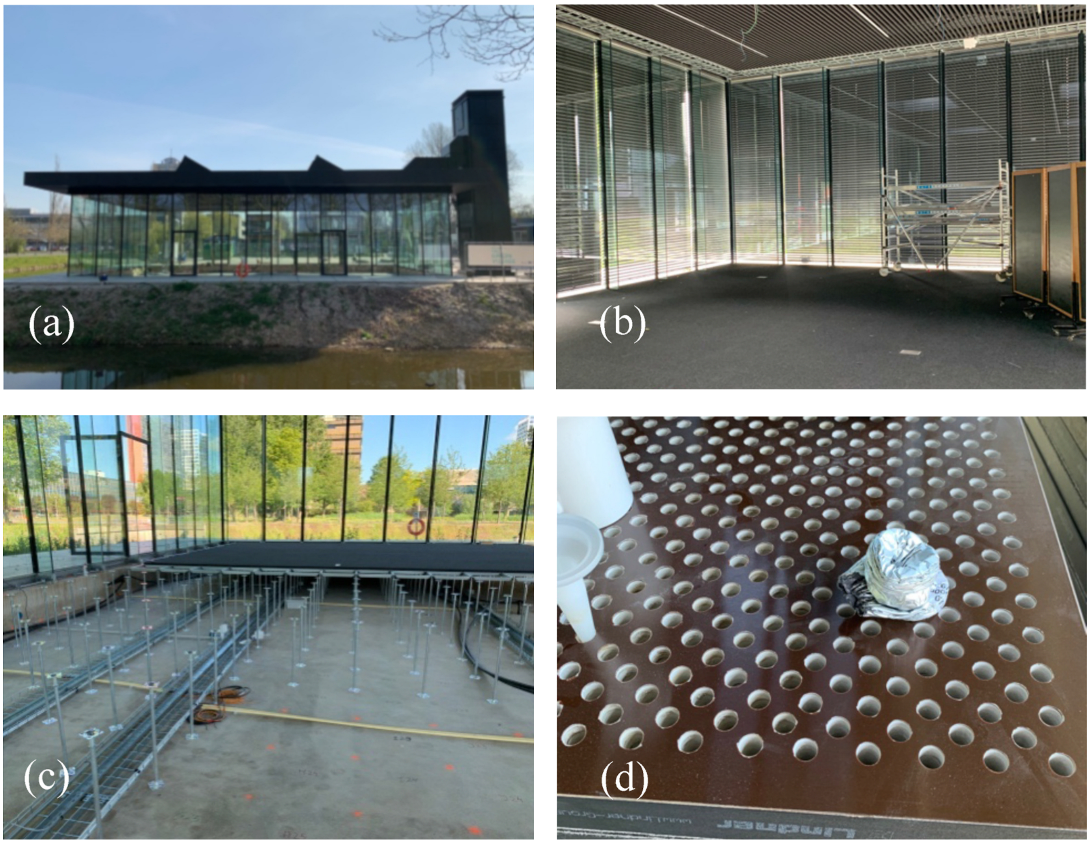

Figure 1: System installed at The Green Village: (a) blinds open, (b) blinds closed, (c) the basement floor, and (d) the design of the tiles.

part of the solar irradiance. Therefore, the materials and dimensions considered in the design directly affect the system's performance. To model the system dynamics, we rely on the law of conservation of energy while considering a nonlinear and a linear formulation for control purposes, as shown in the two following subsections.

2.1 Nonlinear modeling

By the Bernoulli's principle [34], the flow rate produced by the chimney depends on the difference between indoor (T_a^k) and outdoor (T_o^k) air temperatures at that time, as shown:

$$\dot{m}^k = \rho \varphi C_\mathrm{d} \sqrt{2gH \frac{|T_\mathrm{a}^k - T_\mathrm{o}^k|}{T_\mathrm{o}^k}} \tag{1}$$

where the superscript k refers to the time step, such that $k = k\Delta t$ and Δt is the time interval. Furthermore, φ is the chimney cross-sectional flow area, C_d the pressure loss coefficient, H the distance between the air inlet and outlet, ρ the specific mass of air, and g the gravitational constant. Note that we assume incompressible flow and no infiltration in (1). Also, for the given setup, $C_\mathrm{d} = 0.57$, according to preliminary CFD simulations.

To determine the time-dependent indoor air temperature (T_a^k), we consider a single fully mixed volume while balancing the heat rates through the zone. Therefore,

$$T_\mathrm{a}^{k+1} = T_\mathrm{a}^k + \left[N^k \dot{q}_\mathrm{p} + u_\mathrm{e}^k \dot{q}_\mathrm{hp} \; + \; u_\mathrm{v}^k \dot{m}^k c_\mathrm{a} \left(T_\mathrm{o}^k - T_\mathrm{a}^k \right) + \sum_{j=1}^{7} h_j^k A_{\mathrm{s},j} \left(T_{\mathrm{s},j}^k - T_\mathrm{a}^k \right) \right] \frac{\Delta t}{C_\mathrm{a}} \tag{2}$$

where N^k is the number of people, $\dot{q}_\mathrm{p}$ is the heat generation per person (100 W), $\dot{q}_\mathrm{hp}$ the nominal heat pump power (10000 W), u_e^k the control fraction for auxiliary heating, u_v^k the control fraction for ventilation, c_a the specific heat of air, C_a the heat capacity of air, h^k the convection coefficient, A_s the heat transfer area, and

T_s^k the temperature of the indoor surfaces. Note that u_c^k and u_e^k assume normalized values, between 0 and 1. Moreover, T_s^k refers to the indoor layer of the four vertical walls ($T_\mathrm{w1,n}^k$, $T_\mathrm{w1,s}^k$ $T_\mathrm{w1,e}^k$, and $T_\mathrm{w1,w}^k$), ceiling (T_c1^k), and two floor layers (T_f1^k, T_f2^k).

Each wall consists of three layers. To illustrate the calculation of the temperature of the three layers, let us refer to the North facade, indicated with the subscript n:

$$T_\mathrm{w1,n}^{k+1} = T_\mathrm{w1,n}^k + \Big[u_\mathrm{s,n}^k I_\mathrm{w,n}^k \tau_\mathrm{w}^2 \alpha_\mathrm{w} + \sigma F\left(\left(T_\mathrm{w2,n}^k\right)^4 - \left(T_\mathrm{w1,n}^k\right)^4\right) + h_\mathrm{w2}^k\left(T_\mathrm{w2,n}^k - T_\mathrm{w1,n}^k\right) + h_\mathrm{w1}^k\left(T_\mathrm{a}^k - T_\mathrm{w1,n}^k\right)\Big]\frac{A_\mathrm{w,n}\Delta t}{C_\mathrm{w}} \tag{3a}$$

$$T_\mathrm{w2,n}^{k+1} = T_\mathrm{w2,n}^k + \Big[u_\mathrm{s,n}^k I_\mathrm{w,n}^k \tau_\mathrm{w} \alpha_\mathrm{w} + \sigma F\left(\left(T_\mathrm{w1,n}^k\right)^4 + \left(T_\mathrm{w3,n}^k\right)^4 - 2\left(T_\mathrm{w2,n}^k\right)^4\right) + h_\mathrm{w2}^k\left(T_\mathrm{w1,n}^k + T_\mathrm{w3,n}^k - 2T_\mathrm{w2,n}^k\right)\Big]\frac{A_\mathrm{w,n}\Delta t}{C_\mathrm{w}} \tag{3b}$$

$$T_\mathrm{w3,n}^{k+1} = T_\mathrm{w3,n}^k + \Big[u_\mathrm{s,n}^k I_\mathrm{w,n}^k \alpha_\mathrm{w} + \sigma F\left(\left(T_\mathrm{w2,n}^k\right)^4 - \left(T_\mathrm{w3,n}^k\right)^4\right) + h_\mathrm{w2}^k\left(T_\mathrm{w2,n}^k - T_\mathrm{w3,n}^k\right) + \sigma\varepsilon_\mathrm{w}\left(\left(T_\mathrm{sky}^k\right)^4 - \left(T_\mathrm{w3,n}^k\right)^4\right) + h_\mathrm{w3}^k\left(T_\mathrm{o}^k - T_\mathrm{w3,n}^k\right)\Big]\frac{A_\mathrm{w,n}\Delta t}{C_\mathrm{w}} \tag{3c}$$

where u_s^k is the control signal for the shading, I_w^k the solar incidence, τ_w the glass transmittance, α_w the absorptance, ε_w the emissivity, σ the Stefan-Boltzmann constant, and F the view factor. Similar to u_c^k and u_e^k, also u_s^k is normalized between 0 and 1. One should note that equations (3a)–(3c) refer to a single orientation (i.e., North). A similar formulation is considered for the remaining facades (South, West, and East) but is here omitted to avoid redundancy.

The ceiling disposes of an external layer (roof), which is separated from the internal ceiling by thermal insulation. The temperature of the ceiling and roof are expressed as:

$$T_\mathrm{c1}^{k+1} = T_\mathrm{c1}^k + \left[\frac{\kappa_\mathrm{c}}{L_\mathrm{c}}\left(T_\mathrm{c2}^k - T_\mathrm{c1}^k\right) + h_\mathrm{c1}^k\left(T_\mathrm{a}^k - T_\mathrm{c1}^k\right)\right]\frac{A_\mathrm{c}\Delta t}{C_\mathrm{c1}} \tag{4a}$$

$$T_\mathrm{c2}^{k+1} = T_\mathrm{c2}^k + \left[u_\mathrm{s,c2} I_\mathrm{c2}^k \alpha_\mathrm{c2} + h_\mathrm{c2}^k\left(T_\mathrm{o}^k - T_\mathrm{c2}^k\right) + \varepsilon_\mathrm{c2}\sigma\left(\left(T_\mathrm{sky}^k\right)^4 - \left(T_\mathrm{c2}^k\right)^4\right) + \frac{\kappa_\mathrm{c}}{L_\mathrm{c}}\left(T_\mathrm{c1}^k - T_\mathrm{c2}^k\right)\right]\frac{A_\mathrm{c}\Delta t}{C_\mathrm{c2}} \tag{4b}$$

where κ is the conduction coefficient and L_c the thickness of insulation between the surfaces. In addition, $u_\mathrm{s,c2}$ refers to the fraction of solar radiation over the roof. However, note that $u_\mathrm{s,c2} = 1$, since there is no shading over the roof. Regarding the bottom of the building, the floor consists of indoor drilled tiles and the basement floor. Therefore,

$$T_\mathrm{f1}^{k+1} = T_\mathrm{f1}^k + \left[\xi^k I_\mathrm{f1}^k \alpha_\mathrm{f1}\tau_\mathrm{w}^3 + h_\mathrm{f1}^k\left(T_\mathrm{a}^k - T_\mathrm{f1}^k\right)\right]\frac{A_\mathrm{f1}\Delta t}{C_\mathrm{f1}} \tag{5a}$$

$$T_\mathrm{f2}^{k+1} = T_\mathrm{f2}^k + \left[\frac{\kappa_\mathrm{f}}{L_\mathrm{f}}\left(T_\mathrm{g}^k - T_\mathrm{f2}^k\right) + h_\mathrm{f2}^k\left(T_\mathrm{a}^k - T_\mathrm{f2}^k\right)\right]\frac{A_\mathrm{f2}\Delta t}{C_\mathrm{f2}} \tag{5b}$$

where ξ^k indicates the fraction of solar radiation that reaches the floor due to the aperture of the shadings ($\xi^k = f(u_\mathrm{s}^k)$). Moreover, T_g^k indicates the ground temperature, and L_f refers to the thickness of insulation between the basement floor and ground. For the thermal insulation, we consider the conductivities $\kappa_\mathrm{c} = 0.167$ and $\kappa_\mathrm{f} = 0.0313$ W/(mK).

This modeling requires expressions for the heat transfer coefficients, which depend on the temperatures, air velocities, and characteristic length [35]. We draw on the correlations presented in Appendix 1 [36]. Additionally, we calculate the solar incidence at the tilted surfaces according to the Perez model [37]. Table 1 summarizes the system dimensions and thermal-physical properties corresponding to the components regarded.

2.2 Linear modeling

The system model considered in Section 2.1 includes nonlinearities such as the radiative heat rates and temperature-based properties. Nevertheless, for the purpose of controlling the system, one can obtain good performance and fast calculation time if considering a proper linearization approach. In this sense, we

Table 1: System zones, corresponding dimensions (X, Y and Z) and properties.

Zone	X [m]	Y [m]	Z [m]	ρ [kg/m^3]	c [J/(kgK)]	α [-]	τ [-]	ε [-]
Chimney	2	2	5	-	-	-	-	-
Indoor air	13.5	22.5	5.2	1.2	1000	-	-	-
Roof	13.5	22.5	0.004	1050	1800	0.870		0.93
Ceiling	13.5	22.5	0.003	7850	500	-	-	-
N-S wall	13.5	5.2	0.010	2470	900	0.085	0.83	0.82
E-W wall	22.5	5.2	0.010	2470	900	0.085	0.83	0.82
Floor	13.5	22.5	0.038	1550	800	0.200	-	-
Basement	13.5	22.5	0.225	2000	840	-	-	-

Table 2: Vectors for the linearized model.

Vector	Meaning	Components
x^k	Temperatures	T^k_{a} $T^k_{\mathrm{w1,n}}$ $T^k_{\mathrm{w2,n}}$ $T^k_{\mathrm{w3,n}}$ $T^k_{\mathrm{w1,s}}$ $T^k_{\mathrm{w2,s}}$ $T^k_{\mathrm{w3,s}}$ $T^k_{\mathrm{w1,e}}$ $T^k_{\mathrm{w2,e}}$ $T^k_{\mathrm{w3,e}}$ $T^k_{\mathrm{w1,w}}$ $T^k_{\mathrm{w2,w}}$ $T^k_{\mathrm{w3,w}}$ T^k_{c1} T^k_{c2} T^k_{f1} T^k_{f2}
u^k	Control inputs	u^k_{e} u^k_{v} $u^k_{\mathrm{s,n}}$ $u^k_{\mathrm{s,s}}$ $u^k_{\mathrm{s,e}}$ $u^k_{\mathrm{s,w}}$ $u_{\mathrm{s,c2}}$
d^k	Disturbances	N^k T^k_{o} T^k_{sky} T^k_{g}

*The subscripts n, s, e, and w, refer to the geographic direction of each facade (North, South, East, and West).

consider curve fitting for the heat transfer coefficients, a linearized radiation coefficient (λ), and airflow rates decoupled from the temperatures, such that:

$$x^{k+1} = \mathcal{A}^k x^k + \mathcal{B}^k u^k + \mathcal{E}^k d^k \tag{6}$$

where x^k, u^k, and d^k are vectors referring to the temperature states, control inputs, and disturbances, while $\mathcal{A}^k$, $\mathcal{B}^k$, and $\mathcal{E}^k$ are matrices for the linear dynamics. Table 2 describes the vectors in (6), while the matrices are provided in Appendix 2.

3 Control design

The controller is designed to maximize the passive energy utilization while satisfying the thermal comfort condition. Such condition is pursued by minimizing the difference between the indoor temperature and a reference temperature for comfort (T^k_{ref}). The desired system performance, therefore, consists of minimizing the demand for energy (i.e., active energy). Therefore, a multi-objective optimization approach is needed to establish trade-off limits. Depending on the nature of the system dynamics (linear or nonlinear) we have implemented two standard centralized structures, named nonlinear model predictive control (NLMPC) and linear model predictive control (LMPC). In addition, in an effort to improve the performance of the aforementioned standard architecture, a hierarchical model predictive control (HMPC) structure that combines nonlinear and linear agents is also considered. Each architecture has its own model, objective function, and optimization strategy, as further presented in the three following sections.

3.1 Linear Model Predictive Control (LMPC)

LMPC considers a quadratic programming optimization problem in which the linearized system (6) is combined with a quadratic objective function with penalizing matrices, as follows:

$$\min_{u} \sum_{i=0}^{N_{\mathrm{p}}-1} \mathcal{Q}^{k+i} \left(T^{k+i}_{\mathrm{a}} - T_{\mathrm{ref}}\right)^2 + \left(u^{k+1} - u_{\mathrm{ref}}\right)^{\mathrm{T}} \mathcal{R} \, \left(u^{k+1} - u_{\mathrm{ref}}\right) + \mathcal{P} \left(T^{k+N_{\mathrm{p}}}_{\mathrm{a}} - T_{\mathrm{ref}}\right)^2 \tag{7}$$

where u_{ref} is the reference state ($u_{\mathrm{ref}} = 1$ for shadings, and $u_{\mathrm{ref}} = 0$ for ventilation), and $\mathcal{Q}^k$, $\mathcal{R}$, and $\mathcal{P}$ are penalizing matrices for the time-dependent temperature, control inputs, and terminal temperature state. In this case, $\mathcal{Q}^k$ is time-varying since it depends on the people occupancy ($\mathcal{Q}^k = 4000$ for occupied periods and $\mathcal{Q}^k = 0$ for the non-occupied periods), $\mathcal{R} = \mathbf{diag}(3, 0.1, 0.1, 0.1, 0.1)$, and $\mathcal{P}$ is determined by the Riccati equation: $\mathcal{P} = \mathbf{idare}(\mathcal{A}^k,\ \mathcal{B}^k,\ \mathcal{Q}^k, \mathcal{R})$. The convexity of LMPC is tested via the Hexian method [38], i.e., by checking at each time step if the eigenvalues of the Hessian matrix are nonnegative.

3.2 Nonlinear Model Predictive Control (NLMPC)

NLMPC is the benchmark for the current analysis since it is based on the most detailed model (the nonlinear model of Section 2.1), which includes most of the system nonlinearities encountered in the physical system. The optimization uses the active-set algorithm for nonlinear constrained optimization in the *fmincon* function from the MATLAB optimization toolbox [39]. The active-set algorithm was selected because of its satisfactory performance, and faster processing time compared to the other algorithms. The optimization problem considers the following objective function for time step k:

$$\min_{u} \sum_{i=1}^{N_\mathrm{p}} \left(T_\mathrm{a}^{k+i} - T_\mathrm{ref}\right)^2 \tag{8}$$

where the index i refers to the prediction step and N_p to the control horizon. For the nonlinear system, the stability is verified in the sense of the Lyapunov equilibrium state, where the cost function of the optimization problem is taken as the Lyapunov function [38].

3.3 Hierarchical Model Predictive Control (HMPC)

NLMPC and LMPC are both centralized architectures, which means that a unique control agent is in charge of all the outputs and the inputs. However, this centralized approach may not properly exploit the different time constants of the thermal chimney and of the solar shadings. Therefore, a hierarchical configuration is proposed to improve the control scalability and computation time while combining both NLMPC and LMPC in a master-slave relation. The HMPC structure is illustrated in Figure 2. HMPC operates with two controllers (two agents), in which the first agent applies LMPC with the role of providing the optimal temperature trajectory (T_traj^k) over long time horizons, and the second agent uses NLMPC with the role of tracking this optimal temperature over short-term horizons. The objective function in the nonlinear controller takes the following form:

$$\min_{u} \sum_{i=1}^{N_\mathrm{p}} \mathcal{Q}\left(T_\mathrm{a}^{k+i} - T_\mathrm{traj}^{k+i}\right)^2 + \mathcal{R}\ \left(u_\mathrm{e}^{k+i-1}\dot{q}_\mathrm{hp}\right)^2 \tag{9}$$

The matrices $\mathcal{Q}$ and $\mathcal{R}$ in (9) have a different meaning as compared to (8), as hereby they are defined to satisfy a maximum deviation, such that $\mathcal{Q} = 0.8$ and $\mathcal{R} = 7.5 \times 10^{-9}$. Tracking the optimal references, though, it is only relevant for non-occupied hours, as for occupied hours the reference temperature (i.e., 21 °C) is assumed. In the linear controller, the optimization uses the following objective function:

$$\min_{u} \sum_{i=0}^{N_\mathrm{p}-1} \left(u^{k+1} - u_\mathrm{ref}\right)^\mathrm{T} \mathcal{R}\ \left(u^{k+1} - u_\mathrm{ref}\right) \tag{10}$$

where $\mathcal{R} = \mathbf{diag}(3, 0.1, 0.1, 0.1, 0.1, 100)$. Note that only the inputs are penalized in (10), while the system outputs are constrained to meet the reference temperature condition.

While defining the temperature trajectory, the HMPC requires a re-optimization strategy in which the control inputs optimized in the LMPC layer are provided as initial guesses to the NLMPC optimization. However, this re-optimization only considers the inputs for ventilation, while the previous inputs for heating are kept. Also, a Kalman filter [40] is considered for updating unmeasurable temperature states ($\widehat{x}_\mathrm{est}$) in the system, as follows:

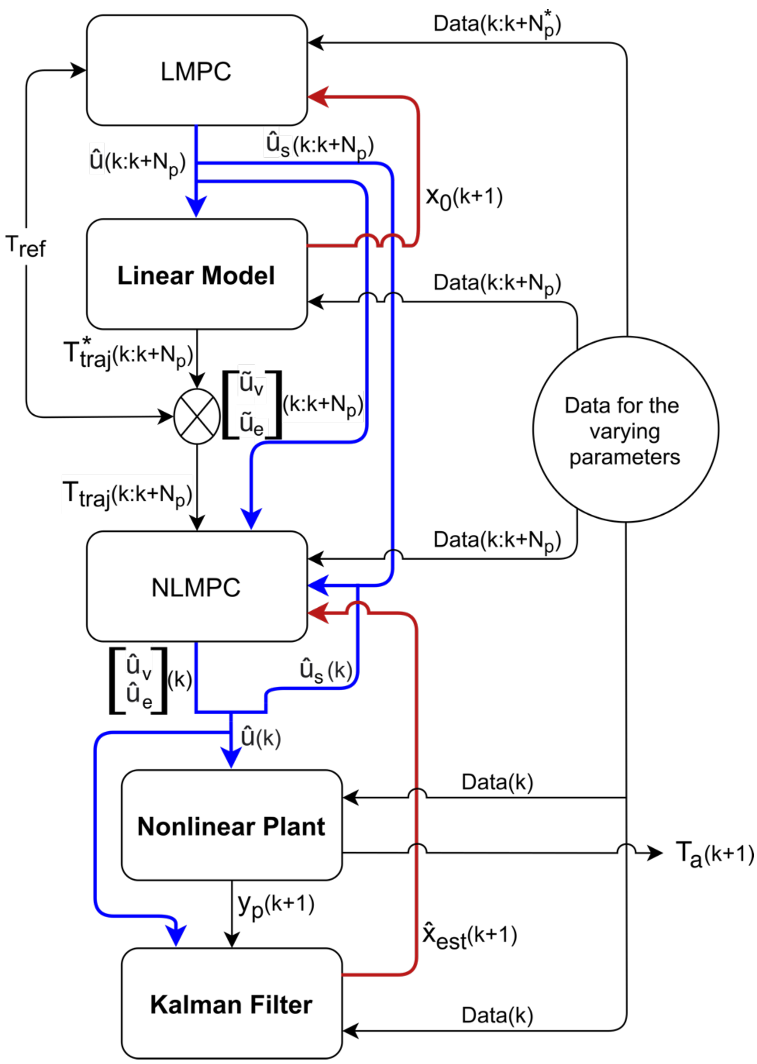

Figure 2: Hierarchical Model Predictive Control (HMPC) structure developed.

Algorithm 1: Kalman filter **MATLAB**

Input: $\widehat{x}_{\text{mod}}(k|k-1)$, $y_{\text{p}}(k)$, $w(k-1)$, $v(k)$, $\mathcal{A}_{k-1}$, $\mathcal{B}_{k-1}$, $\mathcal{C}$
Output: $\widehat{x}_{\text{est}}(k|k)$
  Procedure:
    $r \leftarrow$ **obsv**$(\mathcal{A}_{k-1}, \mathcal{C})$
    $Rank \leftarrow$ **rank**(r)
    $States \leftarrow$ **length**$(\widehat{x}_{\text{mod}}(k|k-1))$
    If $Rank < States$ **then**
      "System not fully observable"
    end if
    $\mathcal{Q}_{k-1} \leftarrow (w(k-1))^2$
    $\mathcal{R}_k \leftarrow (v(k))^2$
    $\mathcal{P}_{k|k-1} \leftarrow \mathcal{B}_{k-1}\mathcal{Q}_{k-1}\mathcal{B}_{k-1}^{\text{T}}$
    $\mathcal{K}_k \leftarrow \mathcal{P}_{k|k-1}\mathcal{C}^{\text{T}}\left(\mathcal{C}\mathcal{P}_{k|k-1}\mathcal{C}^{\text{T}} + \mathcal{R}_k\right)^{-1}$
    $\widehat{x}_{\text{est}}(k|k) \leftarrow \widehat{x}_{\text{mod}}(k|k-1) + \mathcal{K}_k\left(y_{\text{p}}(k) - \mathcal{C}\widehat{x}_{\text{mod}}(k|k-1)\right)$
  return $\widehat{x}_{\text{est}}(k|k)$

---

where $\widehat{x}_{\text{mod}}$ is the temperature state calculated in the model, w and v are white-noise and sensor disturbances, respectively, and y_{p} is the system output, such that $y_{\text{p}}^k = \mathcal{C}x^k$ and $\mathcal{C} = [1, 0, \ldots, 0]$. The vector $\mathcal{C}$ describes the sensor position for system observability and $\mathcal{K}_k$ is the Kalman filter matrix [40].

Table 3: Parameters calibrated for the grey-box model.

Parameter	Initial value	Calibrated value
Z_{c2}	0.0030	0.0026
Z_{f1}	0.038	0.036
α_{f1}	0.200	0.156
Z_{f2}	0.225	0.228
κ_{f}	0.313	0.344
c_{w}	900	792
α_{w}	0.085	0.078
τ_{w}	0.83	0.78
ε_{w}	0.82, 0.16	0.77, 0.13

4 Performance evaluation

To evaluate the performance of the controlled system, we first assess the model's accordance with the measurements collected on site. Next, simulations for the MPC architectures provide key performance indicators such as control accuracy and time response for real-time applications. Finally, we consider a case study to assess the energy savings achieved while comparing HMPC to the rule-based PID controller operating in the actual building.

4.1 Verification of the models

The data collected to verify the accuracy of the models include the temperature states for indoor air and building surfaces, according to the output variables given in Section 3. The airflow induced by the chimney, however, is not verified experimentally, as the actual building is not currently providing such measurements. The airflow rates have, therefore, been verified theoretically by CFD simulations, as previously mentioned. Two testing periods range from April 2 until April 11, 2021; and from May 22 until May 24, 2021. During this period, we established the following operational conditions:

- Solar blinds were fully open.
- No ventilation, windows and doors were closed.
- No occupants and lights were turned off.
- The heat pump was turned off.

The data measured at The Green Village were obtained with a 5-minute sampling time by means of 35 sensors applied to 8 components: 3 for the indoor air, 4 on the ceiling, 2 on each of the north, east, and west-facing interior glazed walls, 4 on the south-facing interior glazed wall, 9 on the deck floor, and 9 on the basement floor. These sensors are strategically distributed over the space, so averaged values are taken to represent the lumped temperature of each component. Moreover, 6 sensors assess the local weather conditions, which include the outside temperature, wind speed, air pressure, relative humidity, and global irradiance. The global irradiance is split in direct beam and diffused horizontal irradiances using the Reindl correlation in TRNSYS 17 [41].

Grey-box identification has been performed to improve the model accuracy, in which 10 model parameters were selected to be calibrated (see Table 3). The outputs from the grey-box model (calibrated values) shown in Table 3 better reflect the system behavior as the model parameters are identified for the current building, while the initial values were obtained for general material descriptions and technical drawings.

The data from the 10-day measurement period in April were selected as training data, while the 3-day measurement period in May 2021 is used to validate the corresponding prediction. Figure 3 presents the comparison between the temperature measurements and the nonlinear model outputs, using the optimized parameters. The verification relies on the VAF (Variance Accounted For) and the NRMSE (Normalized Root-Mean-Square Error), which are presented in Table 4 for all the temperatures assessed. As one can see from Table 4, the model provides a satisfactory prediction.

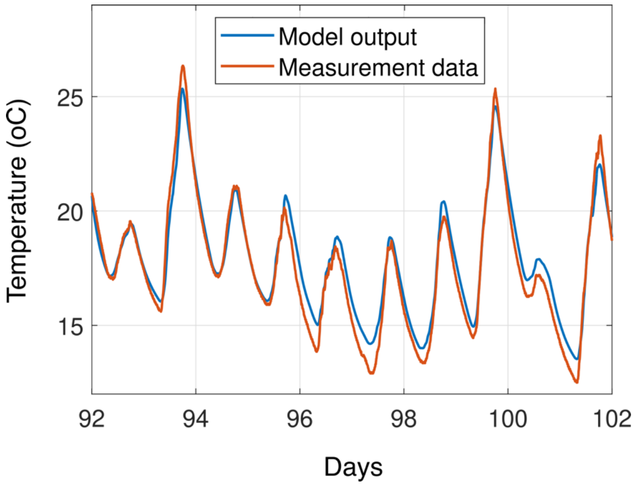

(a)

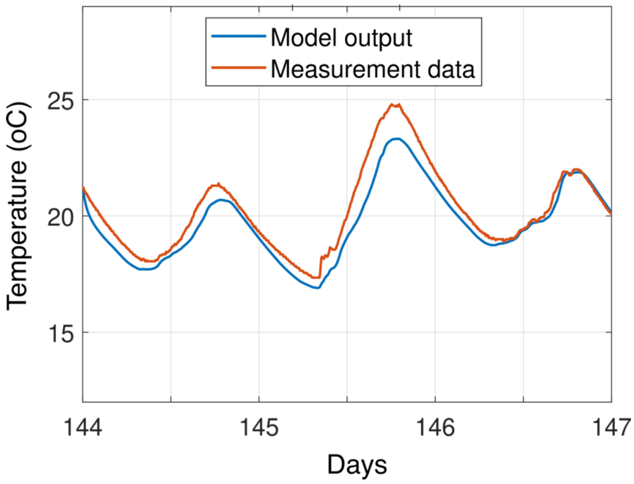

(b)

Figure 3: Temperature profile obtained by experimental and numerical evaluation: (a) training data and (b) training verification.

Table 4: Accordance between temperatures predicted by the model and experimental measurements.

	Training data		Validating data	
Temperature	VAF	NRMSE	VAF	NRMSE
T_{a}	95.8	0.05	93.8	0.10
T_{c1}	94.7	0.05	87.2	0.10
T_{f1}	81.1	0.15	76.9	0.16
T_{f2}	95.9	0.07	89.4	0.09
$T_{\mathrm{w1,n}}$	95.7	0.07	95.8	0.16
$T_{\mathrm{w1,s}}$	96.3	0.05	95.6	0.12
$T_{\mathrm{w1,w}}$	89.5	0.07	89.3	0.10
$T_{\mathrm{w1,e}}$	91.6	0.06	83.5	0.11

4.2 Architecture analysis

To assess the best structure in terms of control performance and computation time, a single objective function is considered by assuming that only passive energy sources are available ($u_{\mathrm{e}}^k = 0$). Therefore, the squared and absolute errors (e) between the reference temperature (T_{ref}^k) and the model's output (T_{a}^k) indicate the control performance, while the computation time of one optimization step (t_{op}) is evaluated for each

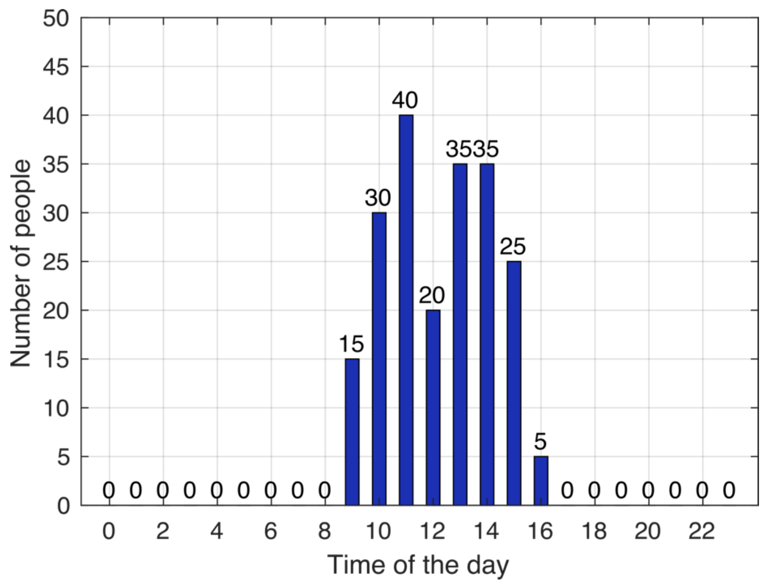

Figure 4: Daily people occupancy schedule.

architecture (LMPC, NLMPC, and HMPC). If these steps take too long, online control becomes impractical. All simulations were performed on an HP ZBook Studio x360 G5, Intel Core i7-8750H processor, with 16 GB of RAM.

The building occupancy is predetermined in Figure 4, where eight occupied hours are selected and applied in each of the MPC structures presented in Section 3. As the occupancy indicates when thermal comfort should be achieved, the periods with occupancy are indicated in the figures as between two black dashed lines. Knowledge of the weather climate data is considered by using the Typical Meteorological Year (TMY) data from EnergyPlus [42]. This data set contains the annual period of historic weather data per hour in Amsterdam, the Netherlands. Weather data from forty consecutive days in Spring (from day 90 to day 130) are selected for the assessment. Such period is chosen because of the varying environmental conditions during spring. In contrast, the summer or winter seasons are predominantly warm or cold. These seasons are likely to result in consistently similar control actions. The disturbance data has an hourly sampling time. We set the MPC time step Δt to one hour as well, analyzing the effects of lowering Δt to 30 minutes since this results in less time available to optimize the inputs.

The analysis starts by plotting the objective function in Figure 5. The circle markers refer to 400 start points, and the color spots refer to the resulting errors, considering a prediction horizon of 2, 4, and 8 days. Moreover, the cross markers indicate the corresponding 400 optimal points. As shown in Figure 5, the indoor temperature variance suggests a minimum and it is, therefore, feasible to optimize. Additionally, the analysis shows that the optima found settles in a single region, which indicates the absence of multiple local optima. Approximately, there is a unique global optimum, and a multi-start procedure is not required which significantly reduces the computation time.

When comparing the NLMPC and LMPC centralized structures, it seems that applying a linearized model with large prediction horizons is beneficial. Such result is shown in Table 5, where % expresses increase/decrease with relation to the centralized structure. In contrast to LMPC, no preparatory decision is considered in NLMPC since the control horizon is limited to 8 hours for feasible computation times. Therefore, the squared error is significantly reduced with LMPC, indicating that making preparatory decisions is effective for future occupied hours. Also, the absolute error remains similar as the LMPC produces a high accuracy when compared to the NLMPC. Additionally, Figure 6 illustrates the indoor temperature profiles obtained by the controllers above.

The hierarchical structure (HMPC) clearly solves this problem as both the squared and absolute errors are reduced significantly. This happens because the NLMPC controller prefers ventilation over shading to affect the air temperature since the indoor temperature response via ventilation is faster. However, the shades have significant effects over the long period due to their influence on the thermal mass, which can be beneficial in future situations. The indoor temperature profile by HMPC is illustrated in Figure 7.

For example, HMPC may prioritize opening the blinds and fully ventilating to cool the inner zone during a semi-warm day, even though a better solution might be to close the blinds and decrease the ventilation

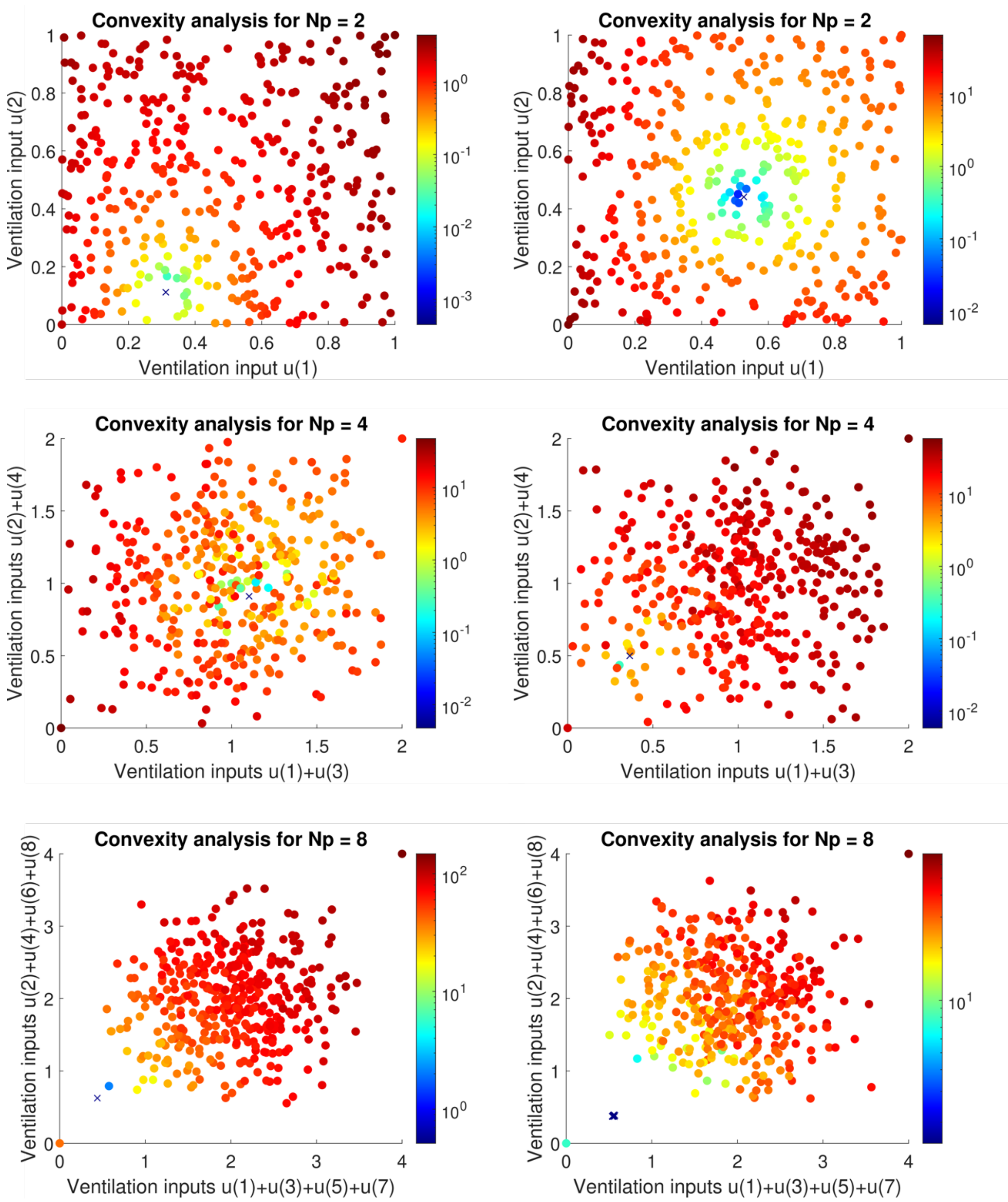

Figure 5: Effects of control inputs on the objective function minimization.

Table 5: MPC architectures assessed and the corresponding performance metrics, where % expresses increase/decrease with relation to the centralized NLMPC.

Architecture	N_p	$\sum e^2$ [K^2]	$\sum e$ [K]	t_op [s]
NLMPC	8	1736	882	30.6
LMPC	24	1373 (−20.9%)	915 (+3.7%)	0.18 (−99.4%)
HMPC	4	1341 (−22.7%)	773 (−12.4%)	2.3 (−92.5%)

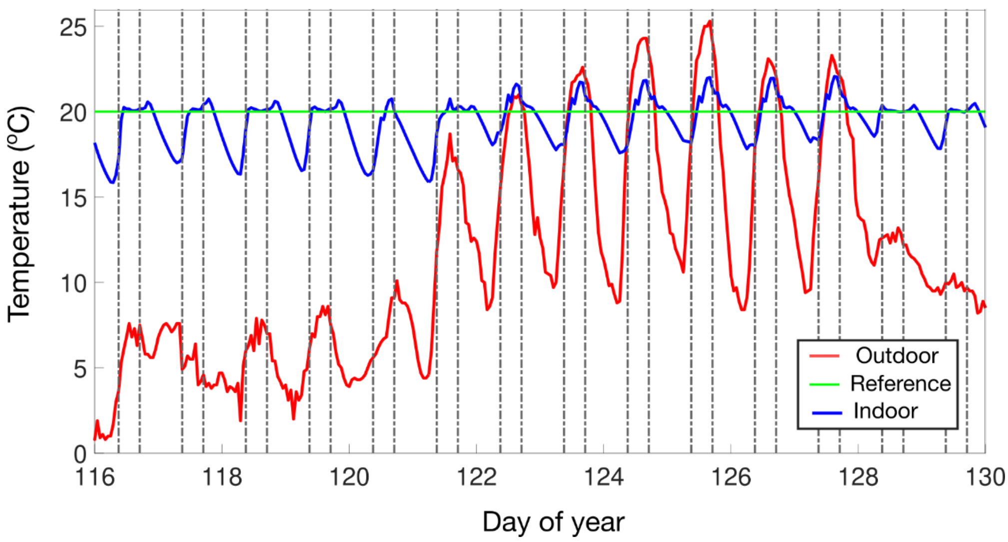

(a) NLMPC

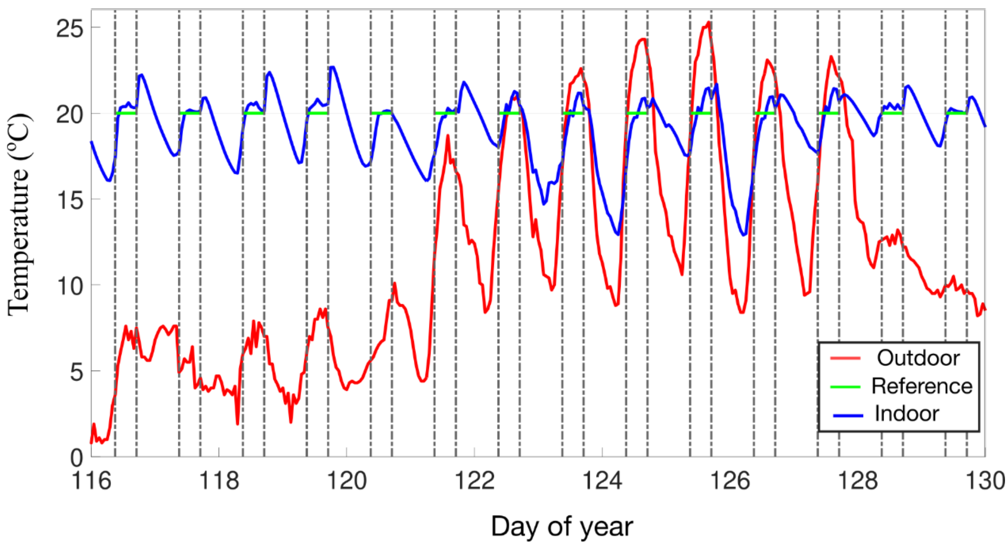

(b) LMPC

Figure 6: (a) Indoor temperature profile for the centralized NLMPC and for (b) LMPC, considering the occupancy profile shown in Figure 4 and typical meteorological year data. The vertical dashed lines stand for the occupied period.

when a period with a warm climate follows. This is a typical scenario that may occur when the blind control inputs are re-optimized on a short horizon, using little knowledge of future disturbances. HMPC solves this problem by assuming that the building's thermal response due to solar irradiance is relatively slow and, therefore, less sensitive to linearizations. Hence, the blind control signals can be optimized on a large horizon by the LMPC agent, using sufficient knowledge of future disturbances. In addition, the re-optimized ventilation control signal can compensate for uncertainties in the short-term predictions. The preservation of high control performance in the short-term is then ensured, while the re-optimization is done faster when only one input type is optimized.

At last, we consider the heat pump demand aiming to make the thermal comfort always achieved. In this case, a multi-objective optimization problem arises, as a conflict occurs between thermal comfort and energy consumption. This is illustrated by constructing the Pareto front of the optimization problem in Figure 8, in which the points contain information of a simulation period of 20 days. In this Pareto front, the standard deviation in relation to the reference temperature and the required auxiliary energy of each simulation period are analyzed. A maximum standard deviation of 0.25 °C is selected, such that 95% of all errors are within 0.5 °C, assuming the error to be a normal distribution. The optimal point chosen is determined by

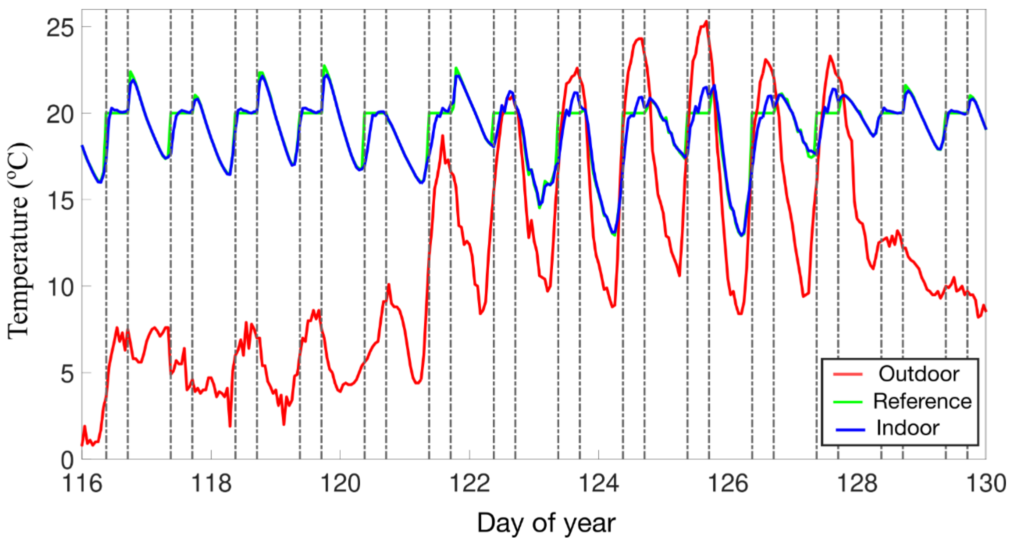

Figure 7: Indoor temperature profile produced by the HMPC considering the occupancy profile shown in Figure 4 and typical meteorological year data. The vertical dashed lines stand for the occupied period and the reference is the optimized trajectory to be followed.

considering both the Pareto front and corresponding computation times. Hence, the corresponding $\mathcal{Q}$ and $\mathcal{R}$ weighting values presented in Section 3.3 are the selected values.

4.3 HMPC versus rule-based PID controller

As the HVAC system installed at The Green Village is currently operated by a rule-based PID controller, we draw on such measurements to evaluate the potential of the developed HMPC architecture for reducing the building's energy consumption while maintaining thermal comfort. The control performance is evaluated keeping the same MPC framework shown in Figure 2. The indoor temperature variance indicates how well thermal comfort is achieved. The system performance is also expressed in terms of the required auxiliary energy, where the energy demanded by the HMPC structure is evaluated considering a maximum deviation of 0.25 °C. The optimized properties in Table 4 are considered.

We evaluate the system performance during the 13-day field experiment, from May 3 to May 15, 2021, in which the measured data have a 5-minute sampling time. During the experimental period, the occupancy in the building is mimicked by 6 electric heaters of 500 W each as, for the simulation, 30 occupants were considered between 9 a.m. and 5 p.m. on weekdays only. Moreover, the direct beam irradiation is omitted after 5 p.m. because of incontrollable shadowing from trees. The reference temperature is set to 21 °C, as this value is also considered by the rule-based controller.

Along with computational complexity considerations, the selection of the control time step and prediction horizon of HMPC should be done based on the control performance, evaluated in terms of absolute and squared errors between the indoor and reference temperature, and based on the total energy demand required to operate the system. The effect of the control time step and the prediction horizon is therefore shown in Figure 10. The results show that lower time steps reduce the errors and energy consumption but increase the computational effort, which presents a more accentuated response. Increasing the prediction horizon also reduces the errors while increasing the computation time but it does not seem to significantly affect the auxiliary energy demand. Therefore, a control time step of 20 minutes and a prediction horizon of 9 hours seem to provide the best control and energy performance. Notably, the performance in terms of errors and energy consumption is quite consistent and it is the computation time that is most sensitive to such parameters. Note that the prediction horizon depends on the time step, such that $N_{\mathrm{p}}\,\#1 = 4\mathrm{h}$ for $\Delta t = 1800$ s, 6h for $\Delta t = 1200$ s , and 8h for $\Delta t = 900$ s. Similarly, $N_{\mathrm{p}}\,\#2 = 6$, 9, 12 hours and $N_{\mathrm{p}}\,\#3 = 8$, 12, 16 hours, for time steps of 1800, 1200, and 900 seconds, respectively.

Figure 9a illustrates the indoor temperature profile achieved by the HMPC structure, which indicates that thermal comfort is well satisfied along the time. In addition, Figure 9b shows the optimal flow rates required to meet the target temperature profile. Note that the same airflow requirement could be supplied with active energy (e.g., mechanical fans), even though such demand is here considered supplied by passive ventilation.

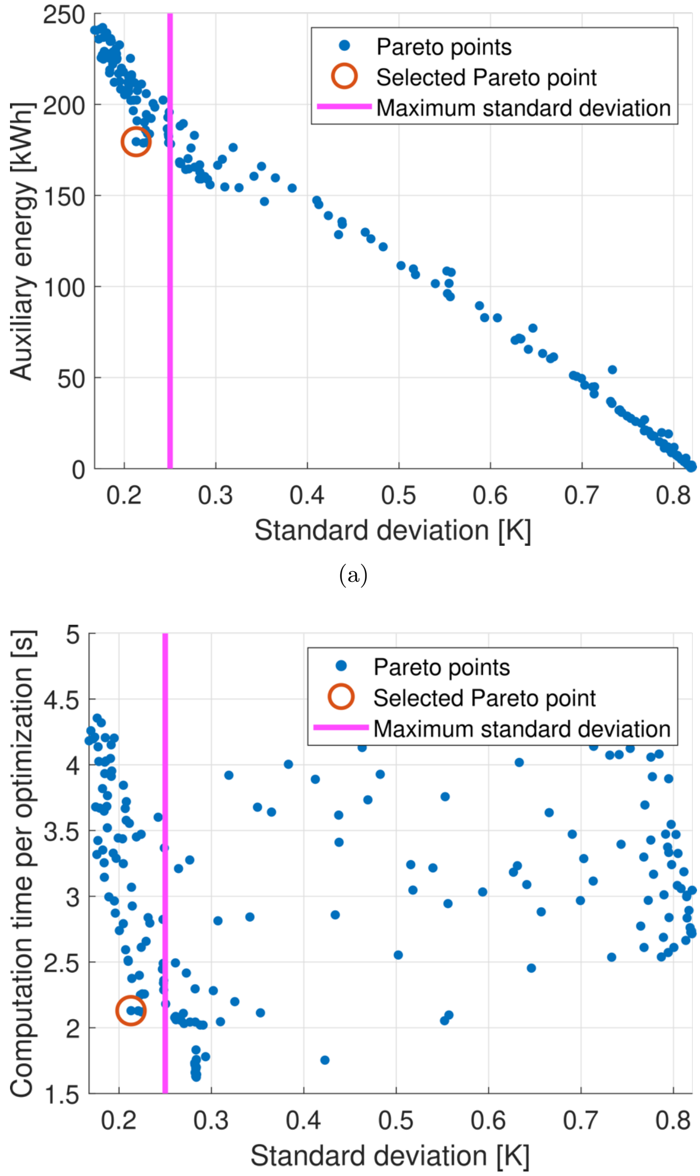

(a)

(b)

Figure 8: Pareto front for the multi-objective optimization problem including as trade-off thermal comfort and auxiliary backup use.

The shades operation is illustrated in Figure 11. As one can see, the shades are closed during warmer days, as expected. The auxiliary energy is mainly supplied during the night shift (see Figure 12). This occurs because the HMPC structure prepares the building for meeting the constraints applied on occupied hours. In the morning, an auxiliary energy peak is required to achieve this constraint. In later hours, the energy gain due to occupancy and the solar incidence is often sufficient. Furthermore, natural ventilation is often applied to cool the building down during the day. Note, however, that the air supply only aims for thermal comfort and not indoor air quality.

For simplicity, a full elaboration on the rule-based PID controller is not provided in this work, but the control objectives considered in this comparison are the same. Figure 13 shows the temperature profile (Figure 13a) and the flow rates (Figure 13b). As shown in Figure 13, the temperature profile in the case of PID control floats around the reference temperature (21 °C) sharper than in the case of HMPC. To reach these temperatures, the heat pump consumed 90 kWh over the 13-day period, while HMPC spent 112 kWh.

As the minimum flow rates for keeping the air quality have not been considered in both control methods, we assume as a reference that a minimum airflow of 0.19 kg/s must be supplied during occupied hours [43]. Next, the energy demand to meet the thermal comfort reference condition (q_{TC}) and the air quality

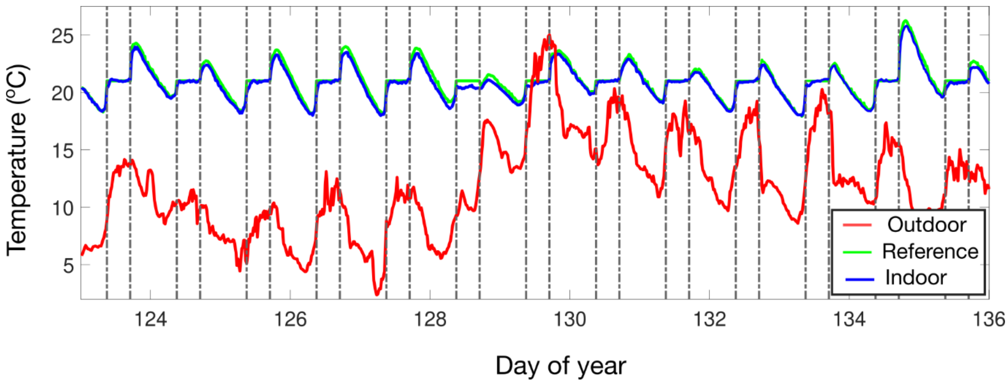

(a)

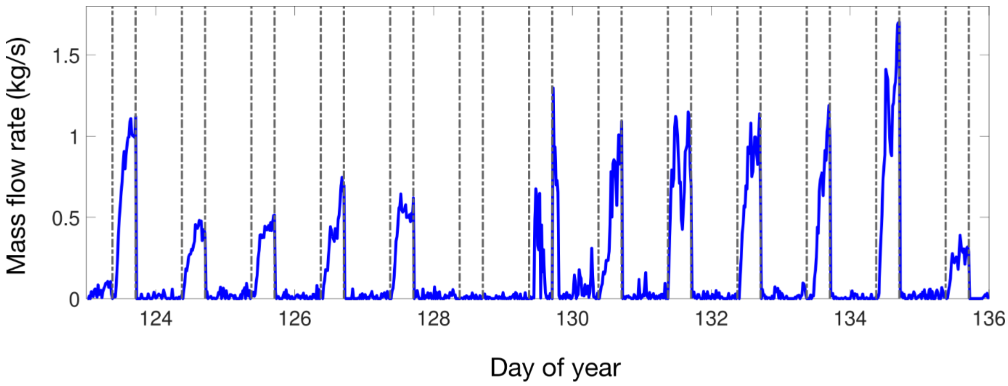

(b)

Figure 9: System operation determined by the HMPC: (a) indoor temperatures and (b) passive ventilation flow rates, where the vertical dashed lines stand for the occupied period.

minimum flow rate (q_{AQ}) is determined as follows:

$$q_{\mathrm{TC}} = \sum_{k=1}^{N} \dot{m}^k c \left|21 - T_{\mathrm{a}}^k\right| \Delta t \tag{11a}$$

$$q_{\mathrm{AQ}} = \sum_{k=1}^{N} (0.19 - \dot{m}^k) c \left|21 - T_{\mathrm{o}}^k\right| \Delta t \qquad \text{if } \dot{m}^k < 0.19 \tag{11b}$$

Equation (11a) determines the required energy to reach the temperature of 21 °C under the ventilation profiles of Figures 9b and 13b. Additionally, (11b) calculates the thermal energy when the required ventilation of 0.19 kg/s is not satisfied. Table 6 provides the results for the energy demands evaluated. The difference between the values shown in Table 6 loosely indicates the control performance, where the HMPC structure appears to achieve better performance than the rule-based controller. For instance, 112 kWh is initially required to achieve the current T_{a} profile of Figure 9a, as opposed to the 90-kWh consumption of the rule-based controller (Figure 13a). However, in the MPC we do not consider the air heat recovery unit lately installed at the building. When considering energy savings, the energy demand decreases to 28 kWh, as shown in the brackets of Table 6. More energy is also required by the PID controller to correct the latter's temperature profile, regardless of the HMPC structure's energy demand for correcting air quality. Therefore, the HMPC structure clearly outperforms the rule-based controller in terms of energy consumption.

Additionally, we assess the energy demand reduction by comparing the yearly energy demand per square meter to the benchmark values of the Almost Energy Neutral Buildings (BENG)-requirements [44]. The HMPC structure and the occupancy scheme of Figure 4 are simulated over the yearly period of TMY data. The building's energy consumption resulted to be 9000 kWh with a standard deviation of 0.27 °C from the reference temperature. Hence, the whole system has a theoretical energy demand of approximately 30 kWh/m^2 per year for thermal control. This energy demand is below the 100–150 kWh/m^2 benchmark and within the 90 kWh/m^2 maximum requirements.

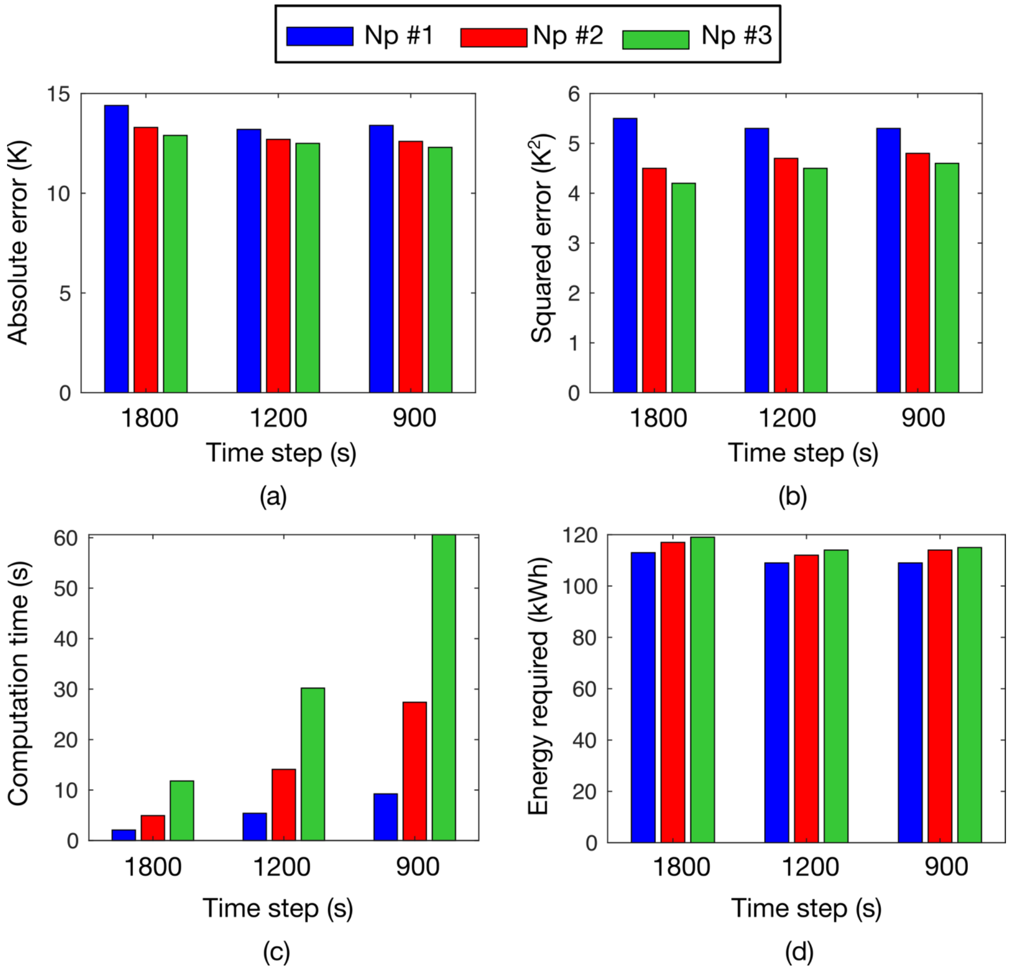

Figure 10: Effect of control time steps and prediction horizons on the MPC performance: (a) absolute error, (b) squared error, (c) computation time of an optimization step, and (d) the auxiliary energy required for system operation. The prediction horizons depend on the time step, such that N_p #1 = 4, 6, 8 hours; N_p #2 = 6, 9, 12 hours; and N_p #3 = 8, 12, 16 hours.

Table 6: Energy demand of the HPMC and rule-based PID for 13 days.

Controller	q_{HP} [kWh]	q_{TC} [kWh]	q_{AQ} [kWh]	$q_{\mathrm{HP}} + q_{\mathrm{TC}} + q_{\mathrm{AQ}}$ [kWh]
HMPC	112 (28*)	4.4	45.6 (11.4*)	162 (43.8*)
PID	90	102.6	4.6	197

*Considering the energy recovery process used by the PID controller.

5 Summary and conclusions

This work has explored predictive control schemes to maximize passive heating and ventilation in indoor spaces, regarding all-glass facades assisted by a thermal chimney and solar shadings. The uniqueness of this configuration calls for optimization-based control methods to realize its best performance, as the proposed controller is shown to address this issue. The analyses have elaborated on the design of predictive models and hierarchical architecture. It has been shown that the resulting controller is suitable for real-time operations, as it shows feasible action times and superior performance when compared to the rule-based PID control operating on site.

We have elaborated on how a set of monitoring sensors could be used to experimentally adjust the simulation models. In fact, it was shown that the adjusted simulation models and the sensor data have a high agreement, i.e., the modeling is appropriate for indoor temperature and HVAC control. The experimental measurements allowed to calibrate the model by optimizing some key parameters, such as the ground

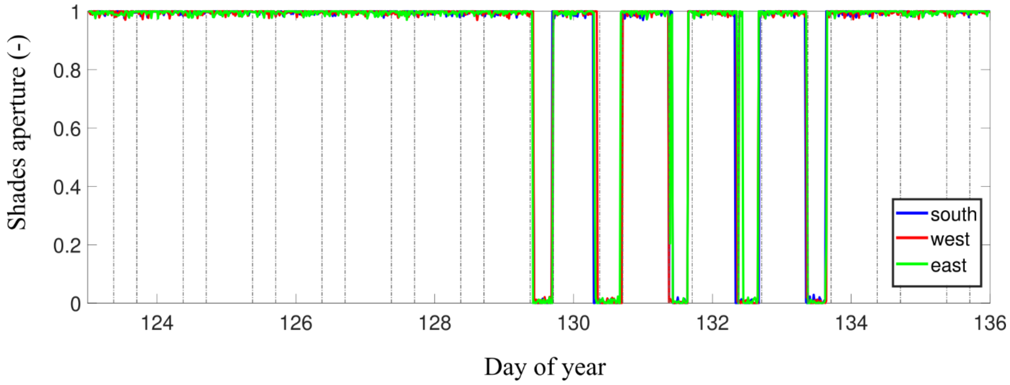

(a)

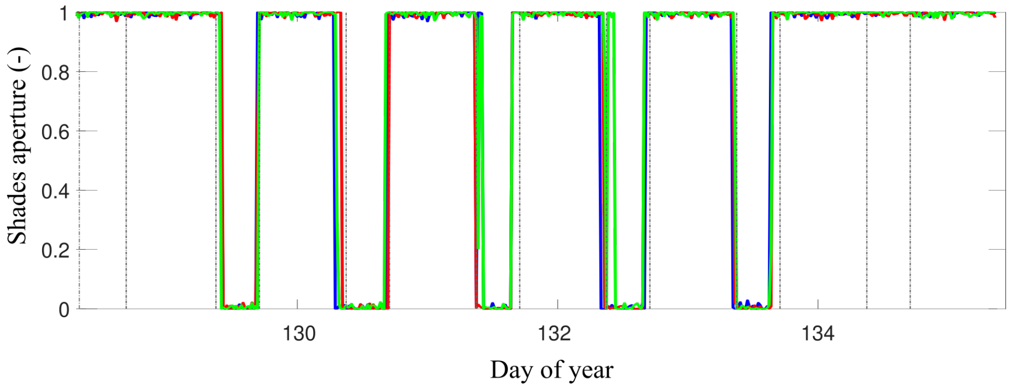

(b)

Figure 11: (a) Opening of blinds in facades south, east, and west, according to the HMPC; and (b) detail of closure of shades at the required times.

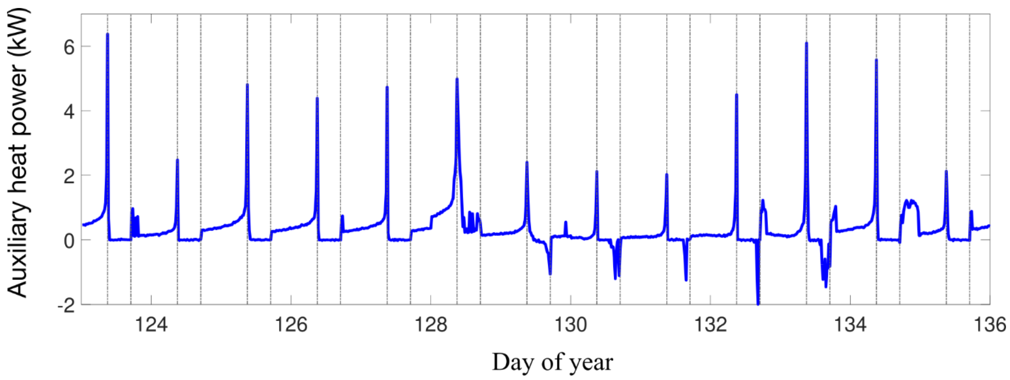

Figure 12: Power profile required by the backup system to reach thermal comfort.

properties, which assures the precision of the models (variance accounted for is superior to 90% in most cases).

As fast processing times are desired, the hierarchical model predictive control (HMPC) structure was considered to handle the transient behavior of each actuator to take the best decision while satisfying the objective of supply thermal comfort. HMPC includes a linear, short-term agent for ventilation control and nonlinear, long-term agents for heating control, resulting in an effective strategy for real-time applications (optimal inputs decision can be easily provided every 30 minutes). When compared to conventional control methods to save energy, the simulations show that the HMPC structure surpasses the PID controller currently operating in the building. Universal applicability is certainly possible in terms of the technologies, system configuration, and methods considered, as the materials were provided by companies in the sector of high-tech sustainable indoor climate. Its universal feasibility, however, depends on trade-offs between costs and energy

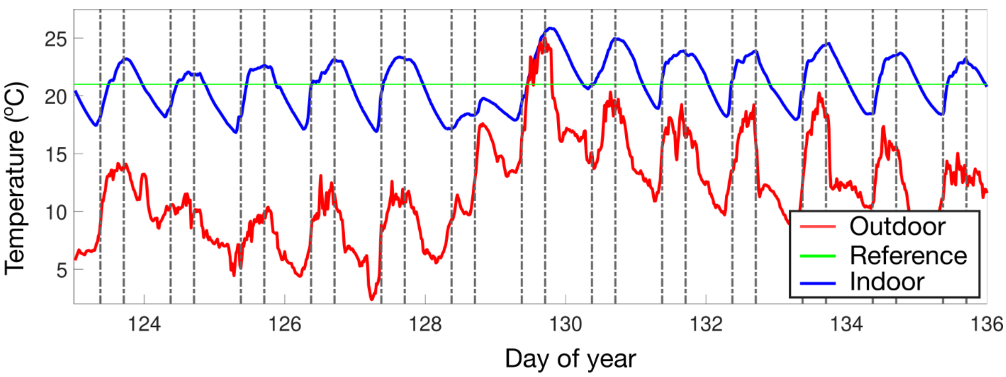

(a)

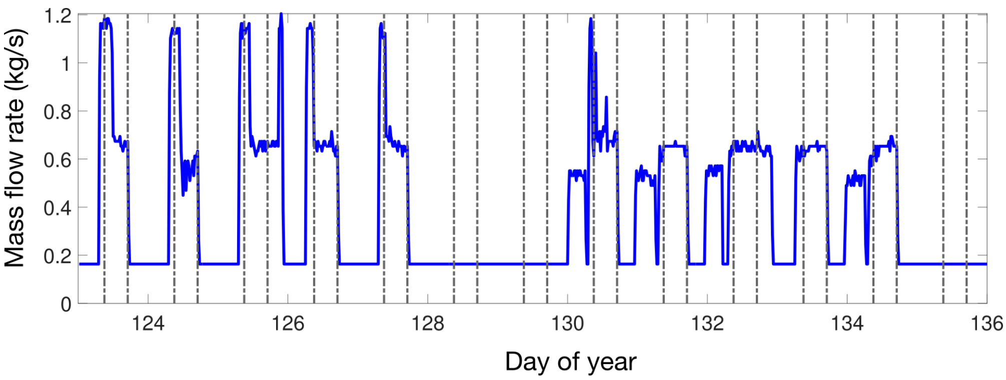

(b)

Figure 13: System operation determined by the rule-based PID control: (a) indoor temperatures and (b) active ventilation flow rates.

performance, which vary on each local condition and require specific studies. Therefore, further studies have been planned to assess the economic features and the consumer market of the sustainable technologies considered. Moreover, future work includes developing control algorithms using real-time computational tools, such as IPOP and C++, for practical implementation. Furthermore, the dynamic prediction of occupancy and the development of data-driven models will be investigated.

Acknowledgments

This work was partly supported by the Netherlands Enterprise Agency (RVO.nl), under the program TKI Urban Energy, grant CONVERGE, by the Research Fund for International scientists, grant 62150610499, by the Key Intergovernmental Special Fund of National Key Research and Development Program, grant 2021YFE098700, and by the Natural Science Foundation of China, grant 62073074.

References

[1] R. Wang, W. Feng, L. Wang and S. Lu, "A comprehensive evaluation of zero energy buildings in cold regions: Actual performance and key technologies of cases from China, the US, and the European Union," *Energy 215*, p. 118992, 2021.

[2] Y. Zhang, T. Tennakoon, Y. H. Chan, K. C. Chan, S. C. Fu, C. Y. Tso, K. M. Yu, B. L. Huang, S. H. Yao, H. H. Qiu and C. Y. H. Chao, "Energy consumption modelling of a passive hybrid system for office buildings in different climates," *Energy 239*, p. 121914, 2022.

[3] C. A. Faulknera, J. E. C. Jr, W. Zuo, D. M. Lorenzetti and M. D. Sohn, "Investigation of HVAC operation strategies for office buildings during COVID-19 pandemic," *Building and Environment 207*, p. 108519, 2022.

[4] F. Harkouss, F. Fardoun and P. H. Biwole, "Passive design optimization of low energy buildings in different climates," *Energy 165*, pp. 519-613, 2018.

[5] R. Wang, S. Lu and W. Feng, “A three-stage optimization methodology for envelope design of passive house considering energy demand, thermal comfort and cost,” *Energy 192*, p. 116723, 2020.

[6] D. Lee, Y.-H. Cho and J.-H. Jo, “Assessment of control strategy of adaptive façades for heating, cooling, lighting energy conservation and glare prevention,” *Energy and Buildings 235*, pp. 110739-18, 2021.

[7] F. Chi, R. Wang, G. Li, L. Xu, Y. Wang and C. Peng, “Integration of sun-tracking shading panels into window system towards maximum energy saving and non-glare daylighting,” *Applied Energy 206*, pp. 114304-21, 2020.

[8] A. Eltaweel and Y. Su, “Controlling venetian blinds based on parametric design; via implementing Grasshopper’s plugins: A case study of an office building in Cairo,” *Energy and Buildings 139*, pp. 31-43, 2017.

[9] N. Kunwar, K. S. Cetin and U. Passe, “Calibration of energy simulation using optimization for buildings with dynamic shading systems,” *Energy and Buildings 236*, pp. 110787-12, 2021.

[10] S. M. Al-Masrani, K. M. Al-Obaidi, N. A. Zalina and M. A. Isma, “Design optimisation of solar shading systems for tropical office buildings: Challenges and future trends,” *Solar Energy 170*, pp. 256-268, 2020.

[11] Y. Chen, Z. Tong and A. Malkawi, “Investigating natural ventilation potentials across the globe: Regional and climatic variations,” *Building and Environment 122*, pp. 386-396, 2017.

[12] H. Zhang, D. Yang, V. W. Y. Tam, Y. Tao, G. Zhang, S. Setunge and L. Shi, “A critical review of combined natural ventilation techniques in sustainable buildings,” *Renewable and Sustainable Energy Reviews 141*, p. 110795, 2021.

[13] N. Monghasemi and A. Vadiee, “A review of solar chimney integrated systems for space heating and cooling application,” *Renewable and Sustainable Energy Reviews 81*, pp. 2714-2730, 2018.

[14] Y. Yao and D. K. Shekhar, “State of the art review on model predictive control (MPC) in Heating Ventilation and Air-Conditioning (HVAC) field,” *Building and Environment 200*, p. 107952, 2021.

[15] J. Drgona, J. Arroyo, I. C. Figueroa, D. Blume, K. Arendt, D. Kim, E. P. Olle, J. Oravec, M. Wetter, D. L. Vrabie and L. Helsen, “All you need to know about model predictive control for buildings,” *Annual Reviews in Control 50*, pp. 190-232, 2020.

[16] J. Joe and P. Karava, “A model predictive control strategy to optimize the performance of radiant floor heating and cooling systems in office buildings,” *Applied Energy 245*, pp. 65-77, 2019.

[17] Y. Chen, Z. Tong, W. Wu, H. Samuelson, A. Malkawi and L. Norford, “Achieving natural ventilation potential in practice: Control schemes and levels of automation,” *Applied Energy 235*, p. 1141–1152, 2019.

[18] J. Xie and A. O. Sawyer, “Simulation-assisted data-driven method for glare control with automated shading systems in office buildings,” *Building and Environment 196*, p. 107801, 2021.

[19] G. Serale, M. Fiorentini, A. Capozzoli, P. Cooper and M. Perino, “Formulation of a model predictive control algorithm to enhance the performance of a latent heat solar thermal system,” *Energy Conversion and Management 173*, pp. 438-449, 2018.

[20] R. Ruusu, S. Cao, B. M. Delgado and A. Hasan, “Direct quantification of multiple-source energy flexibility in a residential building using a new model predictive high-level controller,” *Energy Conversion and Management 180*, pp. 1109-1128, 2019.

[21] S. Yang, M. P. Wan, B. F. Ng, S. Dubey, G. P. Henze, W. Chen, K. Baskaran, “Model predictive control for integrated control of air-conditioning and mechanical ventilation, lighting and shading systems,” *Applied Energy 297*, p. 117112, 2021.

[22] M. Zhang, Q. Wu, J. Wen, X. Xue, Z. Lin and F. Fang, “Real-time optimal operation of integrated electricity and heat system considering reserve provision of large-scale heat pumps,” *Energy 237*, p. 121606, 2021.

[23] G. Lankeshwara, R. Sharma, R. Yan and T. K. Saha, “A hierarchical control scheme for residential air-conditioning loads to provide real-time market services under uncertainties,” *Energy 250*, p. 123796, 2022.

[24] K. Chen and M. Pan, “Operation optimization of combined cooling, heating, and power superstructure system for satisfying demand fluctuation,” *Energy 237*, p. 121599, 2021.

[25] T. Pippia, J. Lago, R. D. Coninck and B. De Schutter, “Scenario-based nonlinear model predictive control for building heating systems,” *Energy and Buildings 247*, p. 111108, 2021.

[26] Y. Zhou, J. Wang, Y. Liu, R. Yan and Y. Ma, “Incorporating deep learning of load predictions to enhance the optimal active energy management of combined cooling, heating and power system,” *Energy 233*, p. 121134, 2021.

[27] J. Drgona, D. Picarda and L. Helsen, “Cloud-based implementation of white-box model predictive control for a GEOTABS office building: A field test demonstration,” *Journal of Process Control 88*, pp. 63-77, 2020.

[28] M. Killian and M. Kozek, “Implementation of cooperative Fuzzy model predictive control for an energy-efficient office building,” *Energy and Buildings 158*, pp. 1404-1416, 2018.

[29] T. Hilliard, L. Swan and Z. Qin, "Experimental implementation of whole building MPC with zone based thermal comfort adjustments," *Building and Environment 125*, pp. 326-338, 2017.

[30] M. Toub, C. R. Reddy, M. Razmara, M. Shahbakhti, R. D. R. III and G. Aniba, "Model-based predictive control for optimal MicroCSP operation integrated with building HVAC systems," *Energy Conversion and Management 199*, p. 111924, 2019.

[31] S. Zhan and A. Chong, "Data requirements and performance evaluation of model predictive control in buildings: A modeling perspective," *Renewable and Sustainable Energy Reviews 142*, p. 110835, 2021.

[32] T. J. Ceha, L. A. de Araujo Passos, S. Baldi and B. De Schutter, "Model Predictive Control for Optimal Integration of a Thermal Chimney and Solar Shaded Building," in *29th Mediterranean Conference on Control and Automation (MED)*, 2021.

[33] The Green Village, "Field lab for sustainable innovation," [Online]. Available: https://thegreenvillage.org/en/. [Accessed 8 May 2021].

[34] P. K. Kundu and I. M. Cohen, Fluid Mechanics, Academic Press, 2004.

[35] F. P. Incropera, D. P. DeWitt, T. L. Bergman and A. S. Lavine, Fundamentals of Heat and Mass Transfer, John Wiley & Sons, 2006.

[36] M. Mirsadeghi, D. Cóstola, B. Blocken and J. Hensen, "Review of external convective heat transfer coefficient models in building energy simulation programs: Implementation and uncertainty," *Applied Thermal Engineering 56*, pp. 134-151, 2013.

[37] J. A. Duffie and W. A. Beckman, Solar Engineering of Thermal Processes, Wiley, 2013.

[38] M. Schwenzer, M. Ay, T. Bergs, D. Abel, "Review on model predictive control: an engineering perspective," *The International Journal of Advanced Manufacturing Technology 117*, p. 1327-1349, 2021.

[39] The MathWorks, *MATLAB Optimization Toolbox*, Massachusetts, United States: The MathWorks, 2020b.

[40] M. Verhaegen and V. Verdult, Filtering and System Identification: A Least Squares Approach, Cambridge University Press, 2007.

[41] Thermal Energy System Specialists, *TRNSYS 17: A Transient System Simulation Program*, Solar Energy Laboratory, University of Wisconsin-Madison, 2009.

[42] EnergyPlus, "Weather Data," [Online]. Available: https://energyplus.net/weather. [Accessed 1 June 2021].

[43] ANSI/ASHRAE, *62.1-2019 Ventilation for Acceptable Indoor Air Quality*, ASHRAE , 2019.

[44] Netherlands Enterprise Agency (RVO), "Energy Performance Indicators - BENG," [Online]. Available: https://www.rvo.nl/onderwerpen/duurzaam-ondernemen/gebouwen/wetten-en-regels/nieuwbouw/energieprestatie-beng/indicatoren. [Accessed 16 November 2021].

Appendix 1

Table 7: Nusselt correlations for the convective heat transfer coefficients.

Nusselt number (Nu)	Author	Condition	Region
$0.037(Re)^{0.8}(Pr)^{0.33}$	Zhukauskas	-	Outside Air Horizontal surface Vertical surface
$0.54(Ra)^{0.25}$	Mc Adams	$T_\mathrm{s} < T_\mathrm{a} \wedge Ra \leq 10^7$	Indoor Air Horizontal surface
$0.15(Ra)^{0.33}$	Mc Adams	$T_\mathrm{s} < T_\mathrm{a} \wedge Ra > 10^7$	Indoor Air Horizontal surface
$0.27(Ra)^{0.25}$	Mc Adams	$T_\mathrm{s} > T_\mathrm{a}$	Indoor Air Horizontal surface
$0.42(Ra)^{0.25}(Pr)^{0.012}\left(\frac{y}{d}\right)^{-0.3}$	MacGregor	-	Wall's cavity Vertical surface
$0.68 + \left[\dfrac{0.670Ra^{0.25}}{1+\left(\frac{0.492}{Pr}\right)^{0.56}}\right]^{0.44}$	Churchill & Chu	$Ra < 10^9$	Indoor Air Vertical surface
$\left[0.825 + \left[\dfrac{0.387Ra^{0.17}}{1+\left(\frac{0.492}{Pr}\right)^{0.56}}\right]^{0.3}\right]^2$	Churchill & Chu	$Ra \geq 10^9$	Indoor Air Vertical surface

Appendix 2

Matrices of coefficients for the linear model

$$
\mathcal{A}^k =
\left[\begin{array}{ccccccccccccccccc}
1-7hA\frac{\Delta t}{C_\mathrm{a}} & hA\frac{\Delta t}{C_\mathrm{a}} & 0 & 0 & hA\frac{\Delta t}{C_\mathrm{a}} & 0 & 0 & hA\frac{\Delta t}{C_\mathrm{a}} & 0 & 0 & hA\frac{\Delta t}{C_\mathrm{a}} & 0 & 0 & hA\frac{\Delta t}{C_\mathrm{a}} & 0 & hA\frac{\Delta t}{C_\mathrm{a}} & hA\frac{\Delta t}{C_\mathrm{a}} \\
hA\frac{\Delta t}{C_\mathrm{w}} & 1-(h+\lambda)A\frac{\Delta t}{C_\mathrm{w}} & \lambda A\frac{\Delta t}{C_\mathrm{w}} & 0 & 0 & 0 & 0 & 0 & 0 & 0 & 0 & 0 & 0 & 0 & 0 & 0 & 0 \\
0 & \lambda A\frac{\Delta t}{C_\mathrm{w}} & 1-2\lambda A\frac{\Delta t}{C_\mathrm{w}} & \lambda A\frac{\Delta t}{C_\mathrm{w}} & 0 & 0 & 0 & 0 & 0 & 0 & 0 & 0 & 0 & 0 & 0 & 0 & 0 \\
0 & 0 & \lambda A\frac{\Delta t}{C_\mathrm{w}} & 1-(2\lambda+h)A\frac{\Delta t}{C_\mathrm{w}} & 0 & 0 & 0 & 0 & 0 & 0 & 0 & 0 & 0 & 0 & 0 & 0 & 0 \\
hA\frac{\Delta t}{C_\mathrm{w}} & 0 & 0 & 0 & 1-(h+\lambda)A\frac{\Delta t}{C_\mathrm{w}} & \lambda A\frac{\Delta t}{C_\mathrm{w}} & 0 & 0 & 0 & 0 & 0 & 0 & 0 & 0 & 0 & 0 & 0 \\
0 & 0 & 0 & 0 & \lambda A\frac{\Delta t}{C_\mathrm{w}} & 1-2\lambda A\frac{\Delta t}{C_\mathrm{w}} & \lambda A\frac{\Delta t}{C_\mathrm{w}} & 0 & 0 & 0 & 0 & 0 & 0 & 0 & 0 & 0 & 0 \\
0 & 0 & 0 & 0 & 0 & \lambda A\frac{\Delta t}{C_\mathrm{w}} & 1-(2\lambda+h)A\frac{\Delta t}{C_\mathrm{w}} & 0 & 0 & 0 & 0 & 0 & 0 & 0 & 0 & 0 & 0 \\
hA\frac{\Delta t}{C_\mathrm{w}} & 0 & 0 & 0 & 0 & 0 & 0 & 1-(h+\lambda)A\frac{\Delta t}{C_\mathrm{w}} & \lambda A\frac{\Delta t}{C_\mathrm{w}} & 0 & 0 & 0 & 0 & 0 & 0 & 0 & 0 \\
0 & 0 & 0 & 0 & 0 & 0 & 0 & \lambda A\frac{\Delta t}{C_\mathrm{w}} & 1-2\lambda A\frac{\Delta t}{C_\mathrm{w}} & \lambda A\frac{\Delta t}{C_\mathrm{w}} & 0 & 0 & 0 & 0 & 0 & 0 & 0 \\
0 & 0 & 0 & 0 & 0 & 0 & 0 & 0 & \lambda A\frac{\Delta t}{C_\mathrm{w}} & 1-(2\lambda+h)A\frac{\Delta t}{C_\mathrm{w}} & 0 & 0 & 0 & 0 & 0 & 0 & 0 \\
hA\frac{\Delta t}{C_\mathrm{w}} & 0 & 0 & 0 & 0 & 0 & 0 & 0 & 0 & 0 & 1-(h+\lambda)A\frac{\Delta t}{C_\mathrm{w}} & \lambda A\frac{\Delta t}{C_\mathrm{w}} & 0 & 0 & 0 & 0 & 0 \\
0 & 0 & 0 & 0 & 0 & 0 & 0 & 0 & 0 & 0 & \lambda A\frac{\Delta t}{C_\mathrm{w}} & 1-2\lambda A\frac{\Delta t}{C_\mathrm{w}} & \lambda A\frac{\Delta t}{C_\mathrm{w}} & 0 & 0 & 0 & 0 \\
0 & 0 & 0 & 0 & 0 & 0 & 0 & 0 & 0 & 0 & 0 & \lambda A\frac{\Delta t}{C_\mathrm{w}} & 1-(2\lambda+h)A\frac{\Delta t}{C_\mathrm{w}} & 0 & 0 & 0 & 0 \\
hA\frac{\Delta t}{C_\mathrm{c1}} & 0 & 0 & 0 & 0 & 0 & 0 & 0 & 0 & 0 & 0 & 0 & 0 & 1-(h+\frac{\kappa}{L})A\frac{\Delta t}{C_\mathrm{c1}} & \frac{\kappa}{L}A\frac{\Delta t}{C_\mathrm{c1}} & 0 & 0 \\
0 & 0 & 0 & 0 & 0 & 0 & 0 & 0 & 0 & 0 & 0 & 0 & 0 & \frac{\kappa}{L}A\frac{\Delta t}{C_\mathrm{c2}} & 1-(\lambda+h+\frac{\kappa}{L})A\frac{\Delta t}{C_\mathrm{c2}} & 0 & 0 \\
hA\frac{\Delta t}{C_\mathrm{f1}} & 0 & 0 & 0 & 0 & 0 & 0 & 0 & 0 & 0 & 0 & 0 & 0 & 0 & 0 & 1-hA\frac{\Delta t}{C_\mathrm{f1}} & 0 \\
hA\frac{\Delta t}{C_\mathrm{f2}} & 0 & 0 & 0 & 0 & 0 & 0 & 0 & 0 & 0 & 0 & 0 & 0 & 0 & 0 & 0 & 1-(h+\frac{\kappa}{L})A\frac{\Delta t}{C_\mathrm{f2}}
\end{array}\right]
$$

$$
\mathcal{B}^k = \begin{bmatrix}
\frac{\dot{q}_{\mathrm{hp}}\Delta t}{C_{\mathrm{a}}} & \frac{\dot{m}c_{\mathrm{a}}\left(T_{\mathrm{o}}-T_{a,0}\right)\Delta t}{C_{\mathrm{a}}} & 0 & 0 & 0 & 0 & 0 \\
0 & 0 & \tau^2\alpha I\frac{A\Delta t}{C_{\mathrm{w}}} & 0 & 0 & 0 & 0 \\
0 & 0 & \tau\alpha I\frac{A\Delta t}{C_{\mathrm{w}}} & 0 & 0 & 0 & 0 \\
0 & 0 & \alpha I\frac{A\Delta t}{C_{\mathrm{w}}} & 0 & 0 & 0 & 0 \\
0 & 0 & 0 & \tau^2\alpha I\frac{A\Delta t}{C_{\mathrm{w}}} & 0 & 0 & 0 \\
0 & 0 & 0 & \tau\alpha I\frac{A\Delta t}{C_{\mathrm{w}}} & 0 & 0 & 0 \\
0 & 0 & 0 & \alpha I\frac{A\Delta t}{C_{\mathrm{w}}} & 0 & 0 & 0 \\
0 & 0 & 0 & 0 & \tau^2\alpha I\frac{A\Delta t}{C_{\mathrm{w}}} & 0 & 0 \\
0 & 0 & 0 & 0 & \tau\alpha I\frac{A\Delta t}{C_{\mathrm{w}}} & 0 & 0 \\
0 & 0 & 0 & 0 & \alpha I\frac{A\Delta t}{C_{\mathrm{w}}} & 0 & 0 \\
0 & 0 & 0 & 0 & 0 & \tau^2\alpha I\frac{A\Delta t}{C_{\mathrm{w}}} & 0 \\
0 & 0 & 0 & 0 & 0 & \tau\alpha I\frac{A\Delta t}{C_{\mathrm{w}}} & 0 \\
0 & 0 & 0 & 0 & 0 & \alpha I\frac{A\Delta t}{C_{\mathrm{w}}} & 0 \\
0 & 0 & 0 & 0 & 0 & 0 & 0 \\
0 & 0 & 0 & 0 & 0 & 0 & \frac{I\alpha A\Delta t}{C_{\mathrm{c2}}} \\
0 & 0 & \xi\frac{\tau^3\alpha IA\Delta t}{C_{\mathrm{f1}}} & \xi\frac{\tau^3\alpha IA\Delta t}{C_{\mathrm{f1}}} & \xi\frac{\tau^3\alpha IA\Delta t}{C_{\mathrm{f1}}} & \xi\frac{\tau^3\alpha IA\Delta t}{C_{\mathrm{f1}}} & 0 \\
0 & 0 & 0 & 0 & 0 & 0 & 0
\end{bmatrix}
$$

$$
\mathcal{E}^k = \begin{bmatrix}
\frac{\dot{q}_{\mathrm{p}}\Delta t}{C_{\mathrm{a}}} & 0 & 0 & 0 \\
0 & 0 & 0 & 0 \\
0 & 0 & 0 & 0 \\
0 & \frac{hA\Delta t}{C_{\mathrm{w}}} & \frac{\lambda A\Delta t}{C_{\mathrm{w}}} & 0 \\
0 & 0 & 0 & 0 \\
0 & 0 & 0 & 0 \\
0 & \frac{hA\Delta t}{C_{\mathrm{w}}} & \frac{\lambda A\Delta t}{C_{\mathrm{w}}} & 0 \\
0 & 0 & 0 & 0 \\
0 & 0 & 0 & 0 \\
0 & \frac{hA\Delta t}{C_{\mathrm{w}}} & \frac{\lambda A\Delta t}{C_{\mathrm{w}}} & 0 \\
0 & 0 & 0 & 0 \\
0 & 0 & 0 & 0 \\
0 & \frac{hA\Delta t}{C_{\mathrm{w}}} & \frac{\lambda A\Delta t}{C_{\mathrm{w}}} & 0 \\
0 & 0 & 0 & 0 \\
0 & \frac{hA\Delta t}{C_{\mathrm{c2}}} & \frac{\lambda A\Delta t}{C_{\mathrm{c2}}} & 0 \\
0 & 0 & 0 & 0 \\
0 & 0 & 0 & \frac{\kappa A\Delta t}{LC_{\mathrm{f2}}}
\end{bmatrix}
$$